Rainfall retrieval over the ocean with spaceborne W-band radar

John M. Haynes,[1] Tristan S. L'Ecuyer,[1] Graeme L. Stephens,[1] Steven D. Miller,[2] Cristian Mitrescu,[3] Norman B. Wood,[1] and Simone Tanelli[4]

Received 15 February 2008; revised 23 September 2008; accepted 24 October 2008; published 4 February 2009.

[1] A method for retrieving precipitation over the ocean using spaceborne W-band (94 GHz) radar is introduced and applied to the CloudSat Cloud Profiling Radar. The method is most applicable to stratiform-type precipitation. Measurements of radar backscatter from the ocean surface are combined with information about surface wind speed and sea surface temperature to derive the path-integrated attenuation through precipitating cloud systems. The scattering and extinction characteristics of raindrops are modeled using a combination of Mie theory (for raindrops) and the discrete dipole approximation (for ice crystals and melting snow), and a model of the melting layer is implemented to represent the transition between ice and liquid water. Backward Monte Carlo modeling is used to model multiple scattering from precipitating hydrometeors between the radar and ocean surface, which is shown to be significant for precipitation rates exceeding 3–5 mm h^{-1}, particularly when precipitating ice is present. An uncertainty analysis is presented and the algorithm is applied to near-global CloudSat observations and compared with other near-global precipitation sources. In the tropics, CloudSat tends to underestimate the heaviest precipitation. It is found that in the middle latitudes, however, CloudSat observes precipitation more often and with greater resulting accumulation than other spaceborne sensors.

Citation: Haynes, J. M., T. S. L'Ecuyer, G. L. Stephens, S. D. Miller, C. Mitrescu, N. B. Wood, and S. Tanelli (2009), Rainfall retrieval over the ocean with spaceborne W-band radar, *J. Geophys. Res.*, *114*, D00A22, doi:10.1029/2008JD009973.

1. Introduction

[2] Precipitation is a key process contributing to the exchange of energy between the Earth's surface and its atmosphere. This energy exchange is an important component of the global water cycle which determines, for example, the availability of water for human use and consumption. Satellite measurements of rainfall have led to great advances in our understanding of how often rain falls and where it falls on the Earth's surface. CloudSat, part of the afternoon A-train constellation of satellites [*Stephens et al.*, 2002], contains the first millimeter wavelength radar designed to observe elements of the Earth's atmosphere from space, providing an opportunity to advance our understand of not only the vertical structure of cloud systems, but the distribution of the rain they produce as well. It is the first active, spaceborne observing system to regularly see precipitation on the planet at latitudes higher than the subtropics.

[3] CloudSat carries the 94 GHz Cloud Profiling Radar (CPR). The CPR is a W-band, nadir-pointing radar system designed for the vertical profiling of hydrometeors in the atmosphere. The performance of the radar since launch is detailed by *Tanelli et al.* [2008]. Although usually optimized for the observations of clouds, high-frequency radars such as the CPR are also highly sensitive to the presence of both solid and liquid precipitation. The effects of attenuation on the radar signal may be significant; the basis of most liquid precipitation retrievals with such radars is related to the principle that attenuation may be utilized as a source of information, rather than a source of geophysical noise.

[4] Several previous studies have examined the feasibility of precipitation retrieval using millimeter wavelength radars. *L'Ecuyer and Stephens* [2002] determined that there was sufficient information in the path-integrated attenuation (PIA) and reflectivity to retrieve profiles of light to moderate rainfall in the tropics. *Matrosov* [2007] demonstrated that the vertical gradient of reflectivity at any height is related to the magnitude of the attenuation at that height, which can then be related back to rain rate.

[5] The basic principle underlying these retrievals is that under single-scatter conditions and assuming perfect knowledge of the drop size distribution in a raining medium, it is possible to use Mie theory to predict the attenuation associated with rain of a given intensity. By

[1]Department of Atmospheric Science, Colorado State University, Fort Collins, Colorado, USA.
[2]Cooperative Institute for Research in the Atmosphere, Colorado State University, Fort Collins, Colorado, USA.
[3]Naval Research Laboratory, Monterey, California, USA.
[4]Jet Propulsion Laboratory, California Institute of Technology, Pasadena, California, USA.

0148-0227/09/2008JD009973

matching the observed attenuation to a set of predicted values, one can then obtain an estimate of the intensity of the precipitation that produced the attenuation. There are several complications to such methods. The first involves separation of the effects of precipitation intensity from those of attenuation; both can lead to variations in the primary measured quantity, radar reflectivity. Knowledge of PIA partially mitigates this uncertainty. Next are the effects of multiple phases of precipitation, since both melting particles and ice phase precipitation contribute to PIA. A third complication is multiple scattering of radiation by raindrops and snowflakes between the target and the antenna, leading to scattering that is greater than the component due to backscattering alone.

[6] The methodology described here attempts to account for each of these complications while still utilizing the basic physical relationship between radar beam attenuation and precipitation rate. In section 2, a method for deriving PIA that is based on the relationship of ocean surface backscattering cross section to wind speed and sea surface temperature is described. Section 3 outlines the basis of the retrieval for warm rain, section 4 details a model of the radar return through the melting level, and section 5 describes calculation of multiple scattering effects utilizing a backward Monte Carlo model of the radiative transfer equation. Section 6 presents the formulation of the full algorithm with an uncertainty analysis, and section 7 describes retrieval results from CloudSat over the near-global oceans, as well as comparison with other precipitation data sets. The last section summarizes the methodology and principle results.

2. Estimation of PIA Over Ocean

[7] Attenuation by hydrometeors can be significant at W band. Consider a column of depth H containing clouds and precipitation. Neglecting melting effects and multiple scattering for the time being, the PIA (dB) is defined as the two-way, integrated extinction due to hydrometeors,

$$PIA = 2\,\psi \int_0^H k_{ext}(s)\mathrm{d}s, \tag{1}$$

where k_{ext} is the height-dependent extinction coefficient due to clouds and precipitation (the value of ψ and other constants are given in Table 1). Here s is defined perpendicular to the surface and increasing with height such that the integration is carried out over all range gates between the surface and H. From the perspective of a W-band spaceborne radar, the surface of the Earth scatters orders of magnitude more radiation than any atmospheric target, and as such is easily detectable unless masked by intervening hydrometeor attenuation. This reduction in surface backscatter provides a means to estimate attenuation. The PIA in a raining column can be estimated through observations of the normalized backscattering cross section of the surface, σ_0, relative to the clear sky, nonattenuated value of this quantity, σ_{clr},

$$PIA = \sigma_{clr} - (\sigma_0 + G), \tag{2}$$

with

$$G = 2\,\psi \int_0^\infty k_{gas}(s)\mathrm{d}s, \tag{3}$$

and k_{gas} is the extinction coefficient due to atmospheric gases. Gaseous attenuation can be significant for millimeter wavelength radar, especially in the relatively moist tropics where it can exceed 5.5 dB (two-way), and its contribution to the surface backscatter must be removed. With knowledge of the atmospheric temperature and moisture structure at the point of measurement, taken here from the ECMWF auxiliary data matched to the observations [*Stephens et al.*, 2008], this contribution can be calculated [*Liebe*, 1985].

[8] The ability to determine PIA therefore depends on knowledge of σ_{clr}. An analysis of σ_{clr} from October 2006 (Figure 1) demonstrates that the spatial variability of this parameter is largest over land surfaces, excluding certain arid regions. This is because backscatter from land surfaces depends on vegetation, surface slope, soil moisture, snow cover, and other factors. For water surfaces, the standard deviation of σ_{clr} is approximately 3.4 dB, but the latitudinal banding suggests a dependence on other physical processes. It will be demonstrated that knowledge of these physical processes allows the variance of σ_{clr} to be reduced, resulting in the ability to estimate PIA within approximately 2 dB. Over land, however, the physical processes controlling σ_{clr} are not easily resolved, and a PIA-based land-surface precipitation retrieval is therefore beyond the scope of this study.

[9] The normalized backscatter of the surface of the ocean can be calculated as a function of viewing angle given measurements of surface wind speed, V, and sea surface temperature, SST [e.g., *Li et al.*, 2005; *Freilich and Vanhoff*, 2003]. The wind speed dependence arises from roughening of the ocean surface by wind-generated waves, and the SST dependence is due to the variation of the Fresnel coefficient of sea water with temperature. Ocean surface backscatter disturbance by raindrops and sea foam effects are neglected. In this study, the relationship between V, SST, and σ_{clr} was established using wind speed measurements derived from the microwave radiances observed by AMSR-E and SST from the ECMWF forecast model. Aqua, the satellite platform containing AMSR-E, flies approximately 1 minute ahead of CloudSat in the A-Train formation, providing nearly simultaneous views of the same scene (albeit with a larger field of view).

[10] AMSR-E derived wind speeds, although useful in clear skies, are contaminated by rainfall and cannot be used in the presence of precipitation. For this reason, ECMWF wind data were also matched to the CloudSat track for comparison purposes. A scatter plot of these two wind speed estimates for a selection of randomly chosen oceanic profiles along the CloudSat track is shown in Figure 2. The scatter is small for clear-sky conditions, but increases in all-sky conditions because AMSR-E radiances are contaminated by rainfall or high values of cloud water path. Given these results, the operational ECMWF winds are used in the retrieval when the presence of precipitation is unknown.

[11] Several months of observations of σ_{clr}, utilizing AMSR-E derived winds and corrected for gaseous attenuation, were gathered for each CloudSat pointing angle

Table 1. List of Variables and Constants

Symbol	Definition	Value
$\alpha_{m,s}$	snowflake mass coefficient	0.07854 kg $m^{-\beta_{m,s}}$
$\alpha_{v,s}$	snowflake velocity coefficient	60.74 kg $m^{-\beta_{v,s}}$
$\alpha_{v,r}$	raindrop velocity coefficient	627.714 kg $m^{-\beta_{v,r}}$
$\beta_{m,s}$	snowflake mass exponent	2.0
$\beta_{v,s}$	snowflake velocity exponent	0.61
$\beta_{v,r}$	raindrop velocity exponent	0.7619
Γ_e	environmental lapse rate	6 K km^{-1}
ϵ	fractional uncertainty in retrieved precipitation rate	
η_o, η_m	backscattering coefficient of spherical, melting particle distribution	
η_{mc}	backscattering coefficient from Monte Carlo calculations	
ρ_m, ρ_s, ρ_v	density of melting particle, snowflake, water vapor	
ρ_i	density of solid ice	917 kg m^{-3}
ρ_w	density of liquid water	1000 kg m^{-3}
σ_0	surface backscattering cross section	
σ_{clr}	clear-sky surface backscattering cross section	
σ_g	standard deviation of D_g	$\ln(\sigma_g) = 0.3$
χ	factor to remove attenuation near the surface	
ψ	conversion factor	10/ln(10)
$A(r)$	attenuation from the satellite to range r	
A_λ	*Marshall and Palmer* [1948] parameter	4100 m^{-1} (mm $h^{-1})^{0.21}$
B_λ	*Marshall and Palmer* [1948] parameter	−0.21
A_{fm}	ventilation exponent	1.7
A_r	area ratio of bullet rosettes	
B_{fm}	ventilation coefficient	33.0 $cm^{-0.7}$
C	radar calibration constant	
CWC	cloud water content	
D_Γ	characteristic diameter of modified gamma distribution	
D, D_m, D_s	diameter of raindrop, melting particle, snowflake	
D_g	geometric mean cloud particle diameter	20 μm
D_{liq}, D_{tot}	depth of liquid layer, precipitating layer	
$D_{\max}$	maximum particle dimension of bullet rosettes	
D_v	water vapor diffusivity in air	2.77 × 10^{-7} m^3 cm^{-1} s^{-1}
f	mass fraction of melt water in particle	
f_a, f_w, f_s	volume fraction of air, liquid water, snow	
f_c	cutoff value for f_{tot}	0.25
f_{tot}	total melted fraction of particle distribution	
G	gaseous attenuation	
H, H_{CTL}, H_f, H_{sig}	height of precipitating column, lowest layer cloud top, freezing level, penetration of 10 dBZ echo through freezing level	
K	radar dielectric constant	$\lvert K\rvert^2 = 0.75$
K_T	thermal conductivity of air at 273.15 K	2.4 × 10^{-4} J cm^{-1} K^{-1} s^{-1}
k_{ext}, k_{gas}	extinction coefficient of hydrometeors, atmospheric gases	
$k_{ext,0}$, $k_{sca,0}$	extinction, scattering coefficient of spherical particle distribution	
$k_{ext,d}$, $k_{sca,d}$	extinction, scattering coefficient of bullet rosette particle distribution	
$k_{ext,m}$, $k_{sca,m}$	extinction, scattering coefficient of melting particle distribution	
L_f	latent heat of fusion	3.34 × 10^5 J kg^{-1}
L_v	latent heat or vaporization	2.5 × 10^6 J kg^{-1}
dm_{cond}	mass of vapor condensed onto particle surface	
m, m_s, m_w	mass of raindrop, snowflake, melt water	
N, N_c, N_m, N_s	size distribution of rain, cloud drops, melting particles, snowflakes	
N_0	intercept parameter of exponential distribution	8 × 10^6 m^{-4}
N_Γ	intercept parameter of modified gamma distribution	
P_o	phase function for spherical particles	
P_o, P_d, P_m	distribution-integrated phase function for spherical particles, bullet rosettes, melting particles	
P_r, P_t	radar receive, transmit power	
PIA	path-integrated attenuation due to hydrometeor	
PIA_{app}	apparent path-integrated attenuation	
dQ	energy transferred to particle surface from environment	
Q_{sca}, Q_{ext}	scattering, extinction efficiency	
R	precipitation rate	
SST	sea surface temperature	
U_m, U_r, U_s	fall speed of melting particle, raindrop, snowflake	
V	ocean surface wind speed	
w	large-scale vertical velocity	
Z_e, Z_{mc}	radar reflectivity calculated from hybrid approach, Monte Carlo	
Z_{ns}	measured near-surface radar reflectivity	
Z_u	derived unattenuated radar reflectivity	

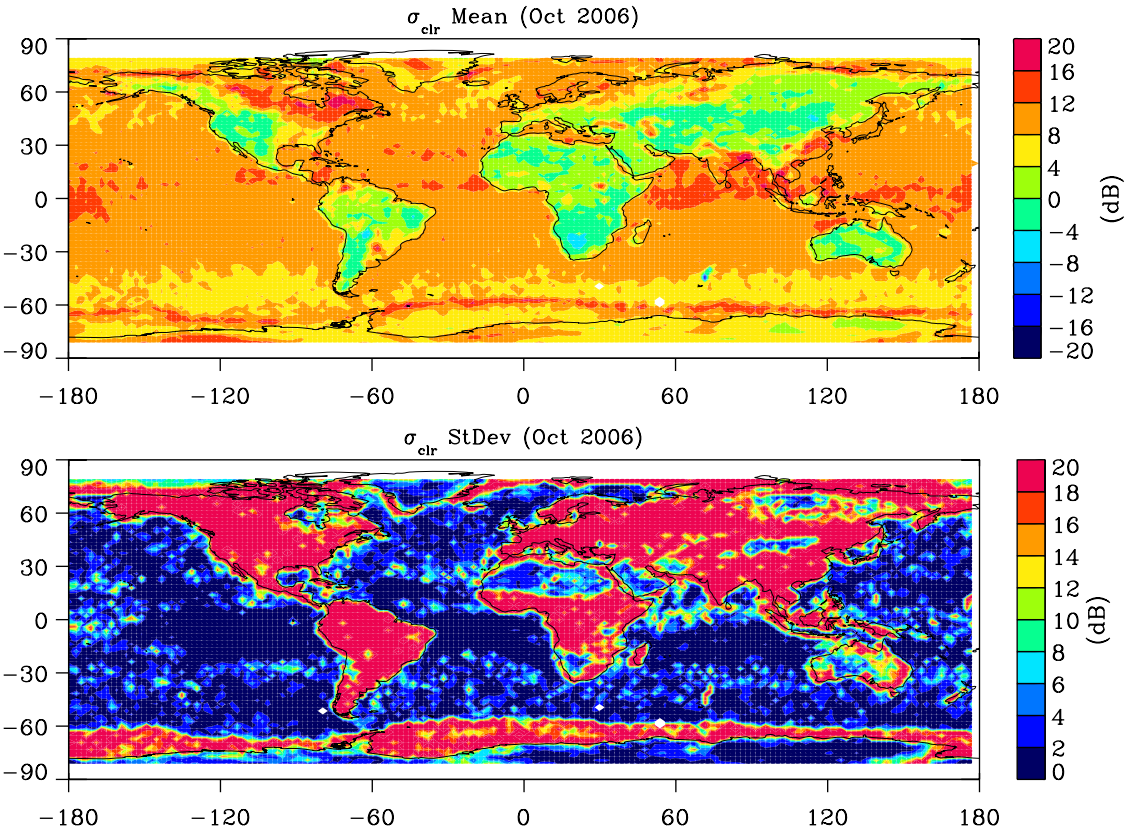

Figure 1. (top) Mean and (bottom) standard deviation of clear-sky ocean surface normalized backscattering cross section for October 2006.

epoch (CloudSat currently points 0.16° off nadir, and only results from this epoch are discussed here) and a range of SSTs. The resulting relationships between σ_{clr} and V largely agree with the parameterization described by *Li et al.* [2005] and have standard deviations varying between approximately 0.5 and 2.5 dB, as shown in Figure 3. Backscatter off the ocean surface is largest for small wind speeds, where it becomes quasi-specular. As wind speed increases, surface roughening results in scattering of power outside the field of view of the radar receiver, and σ_{clr} decreases accordingly. The wind speed dependence is visible in Figure 1; ocean values of σ_{clr} are relatively small, for example, between 40 and 60° S latitude, where the circumpolar vortex produces strong surface winds resulting in a roughened sea

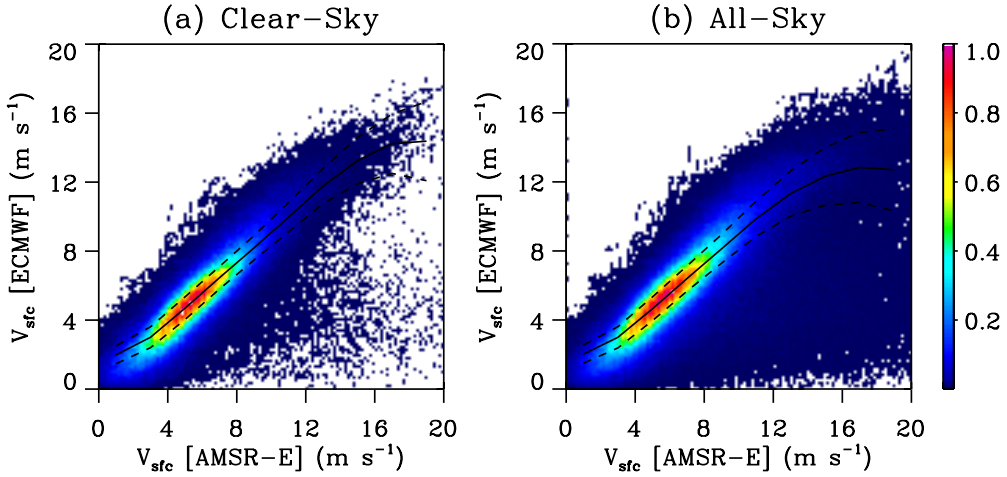

Figure 2. Wind speed derived from AMSR-E microwave estimate versus that of the ECMWF operational forecast model for (a) clear-sky conditions and (b) all-sky conditions. The mean and standard deviations are shown in solid and dashed lines, respectively. Colors indicate normalized frequency of occurrence.

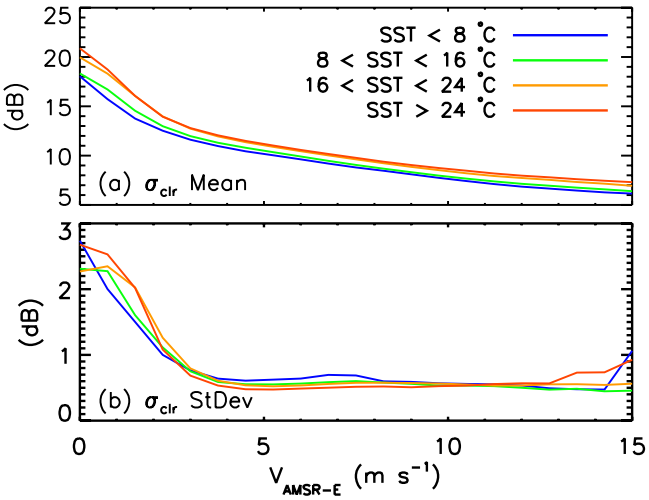

Figure 3. Relationship between AMSR-E derived wind speed and σ_{clr} as a function of SST. (a) Mean relationship and (b) standard deviation.

surface. The tropical and subtropical oceans, by contrast, have generally calm seas with relatively high values of σ_{clr}.

3. Retrieval for Warm Rain

[12] Neglecting melting effects and multiple scattering (which will be dealt with in sections 4 and 5), the basis of a PIA-based precipitation retrieval lies in the implied relationship between the observed attenuated surface backscatter, σ_0, and the integrated extinction coefficient, k_{ext}. Assuming a constant warm rain profile between the surface and a height H above the surface, (1) and (2) may be combined to obtain

$$\sigma_0 = \sigma_{clr} - (G + 2\,\psi k_{ext} H)\ . \tag{4}$$

In an idealized case, H may be considered the lesser of the height of the melting layer and cloud top height, as determined from the reflectivity signature. For CloudSat, the cloud top height is determined from the 2B-GEOPROF cloud mask. The assumption of a uniform vertical rain profile is most applicable to stratiform-type rain, as addressed in section 6.

[13] The extinction coefficient, k_{ext}, can in turn be related to precipitation rate, R, given knowledge of the drop size distribution (DSD) of the raindrops. Without a priori knowledge of the DSD for the myriad of scenes that the radar may observe, for simplicity we assume a raindrop size distribution given by the classic *Marshall and Palmer* [1948] exponential relation,

$$\begin{aligned} N(D) &= N_0 \exp(-\lambda D) \\ \lambda &= A_\lambda R^{B_\lambda}, \end{aligned} \tag{5}$$

where N is the particle number concentration, and other constants are defined in Table 1. Cloud water is considered wherever rain is present; cloud water content (CWC) is taken to be a constant 0.15 g m^{-3} for $R > 5$ mm h^{-1}, decreasing linearly to 0.1 g m^{-3} as R approaches zero. These values follow from independent pixel-scale estimates of the cloud liquid water path derived from the MODIS collection 5 cloud products [*Platnick et al.*, 2003] collocated with raining CPR pixels (determined as described below) where the 10.8 μm brightness temperature is greater than 270 K and no ice is present. Following *Austin and Stephens* [2001], a log-normal distribution of cloud water is assumed, with the total concentration of cloud drops given by

$$\begin{aligned} N_c(D) = &\frac{12\ CWC}{\rho_w \sqrt{2\pi^3}\,(\ln \sigma_g) D_g^3\, D} \\ &\times \exp\left[-\frac{1}{2}\left(\left[\frac{\ln(D/D_g)}{\ln \sigma_g}\right]^2 + [3 \ln \sigma_g]^2\right)\right], \end{aligned} \tag{6}$$

where ρ_w is the density of liquid water, D_g is the geometric mean particle diameter, and ln σ_g is the log of the geometric standard deviation [*Miles et al.*, 2000].

[14] For spherical particles,

$$k_{ext} = \frac{\pi}{4} \int_0^\infty Q_{ext}(D)\,[N(D) + N_c(D)]\,D^2 \mathrm{d}D\ , \tag{7}$$

where Q_{ext} is the extinction efficiency obtained from Mie theory for a large range of particle sizes [*Bohren and Huffman*, 1983]. This relationship is shown at a variety of common radar frequencies in Figure 4. The viability of this approach for cloud radars (such as the W-band CPR) is immediately apparent; higher-frequency radars experience more attenuation for a given rain intensity than lower frequency radars. Furthermore, the sensitivity of attenuation to rainfall is greatest for small R, indicating that PIA based rainfall retrievals work best for light rainfall. It is noteworthy that this approach is not applicable to radars with frequencies lower than Ku band (about 12–18 GHz) as the influence of rain on the surface signal will be smaller than the uncertainty in the measurement of σ_0.

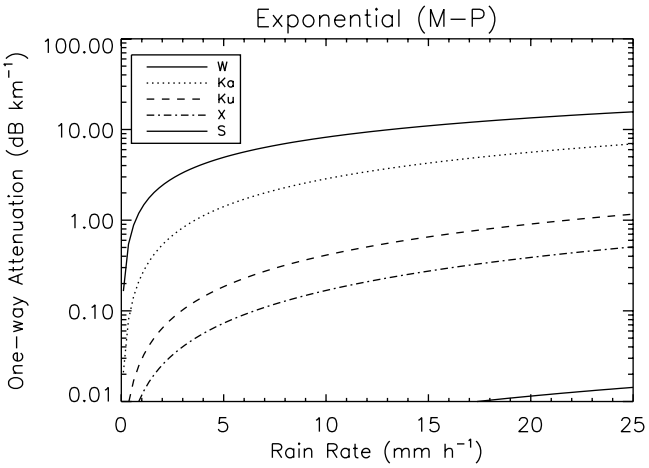

Figure 4. Attenuation coefficients for a Marshall-Palmer-type distribution of rainfall at a variety of common radar bands as indicated by their IEEE identification. The CloudSat CPR is a W-band radar.

Table 2. Rain Likelihood as Defined by Unattenuated Near-Surface Reflectivity Z_u

Condition	Z_u Range (dB)
Rain definite	>0
Rain probable	−7.5 to 0
Rain possible	−15 to −7.5
Snow definite	> −5
Snow possible	−15 to −5
No precipitation	< −15

[15] The combination of equations (4) through (7) provides the relationship between σ_0 and R, whose solution is given by

$$\sigma_0 = \sigma_{clr}(V, SST) - \left(G + \frac{\pi \psi H}{2} \int_0^\infty Q_{ext}(D) \left[N_0 \exp(-A_\lambda R^{B_\lambda} D) + N_c(D) \right] D^2 \mathrm{d}D \right). \quad (8)$$

[16] Thus (8) indicates that given knowledge of the ocean surface wind speed, SST, depth of the raining column, column temperature and humidity (to derive the gaseous attenuation), and an observation of σ_0, one can derive the rain rate for that profile. This formulation neglects multiple scattering and ice phase precipitation within the radar beam, and as such is only useful in those cases with purely liquid precipitation and R less than approximately 3 mm h^{-1}, as described in coming sections. An accurate model of frozen and melting particles is required to expand the applicability of this algorithm beyond rain-only scenes.

[17] The CPR is an excellent detector of precipitation because of its high frequency and sensitivity; in fact, the instrument is sufficiently sensitive to the presence of small water droplets that even the incipient stages of precipitation formation can be detected [*Stephens and Haynes*, 2007]. The detection problem is distinct from quantification; equation (8), for example, should only be applied in those instances when rain is known to occur. Precipitation detection is based on the concept that increasing values of unattenuated reflectivity near the surface are associated with increasing likelihood of surface precipitation. Since CPR power returns in the lowest bins often contain surface contamination [*Tanelli et al.*, 2008], the reflectivity in the fourth bin (between 600 and 840 m above the surface) is considered. The unattenuated reflectivity in this bin, Z_u, is simply the sum of the observed reflectivity, Z_{ns}, and the contributions from PIA and gaseous attenuation, such that

$$Z_u = Z_{ns} + PIA \cdot \chi + G. \quad (9)$$

The PIA has been modified by a factor χ to remove attenuation in the radar column at levels lower than the near-surface range bin at height H_{ns}; χ may be set to $(H - H_{ns})/H$ in the presence of uniform, single-phase precipitation.

[18] Threshold values of Z_u have been chosen to indicate the likelihood of precipitation, as shown in Table 2. For example, using the precipitation and cloud water distribution described in this section, an unattenuated near-surface reflectivity of 0 dB or higher is nearly certain to produce appreciable rain, corresponding to about 0.03 mm h^{-1}. To produce the same precipitation rate in pure snow, DDA calculations (see section 5) suggest only −5 dB is required, so the threshold is adjusted accordingly when the ECMWF operation temperature profile indicates the entire atmosphere is colder than 0° C. For both rain and snow, Z_u less than −15 dB is unlikely to be associated with precipitation except, perhaps, the very lightest of drizzle [e.g., *Stephens and Wood*, 2007]. Intermediate values between these limits are assigned increasing likelihoods of precipitation occurrence.

4. Melting Layer Effects on PIA

[19] Although it has been assumed that precipitation rate is constant with height, this does not necessarily mean that the profile of hydrometeor extinction need be constant. Precipitation may begin as snow, fall through a melting layer, and reach the surface as liquid. To simulate this effect, a model of the melting layer is developed that follows a snowflake as it makes the transition to raindrop. This model follows the general methodology employed by *Klaassen* [1988], *Hardaker et al.* [1995], *Szyrmer and Zawadzki* [1999], and others, with one chief exception: the discrete dipole approximation (DDA) is used to represent the radiative properties of snow and weight the radiative properties of the particles during the beginning stages of melting. For now we will consider all hydrometeors as spheres, and will leave the DDA correction to be discussed later.

4.1. Microphysical Model

[20] The mass of any given raindrop and its corresponding melting particle and snow aggregate (m, m_m, and m_s) are taken to be equal throughout its lifetime, neglecting evaporation and the small amount of water that may collect on the particle owing to vapor diffusion. Coalescence and drop breakup are neglected following *Fabry and Zawadzki* [1995], who found that these effects, while present, had little contribution to radar reflectivity during the melting process. With these assumptions,

$$\rho_w D^3 = \rho_m D_m^3 = \rho_s D_s^3, \quad (10)$$

where ρ_w is the density of liquid water, D is the particle melted diameter, ρ_m and ρ_s are the densities of the melting particle and snowflake, and D_m and D_s are the diameters of the same. The mass of snowflakes is taken to follow the power-law relation

$$m_s = \alpha_{m,s} D_s^{\beta_{m,s}}, \quad (11)$$

with D_s and ρ_s (truncated between 5 and 917 kg m^{-3}) following from (10) and (11). It is further assumed that the density of the melting particle is related to the inverse of the mass fraction of melt water in the particle, f,

$$f = \frac{m_w}{\rho_w D^3} \quad (12)$$

$$\rho_m = \frac{\rho_s \rho_w}{f \rho_s + (1 - f) \rho_w}, \quad (13)$$

where m_w is the mass of melt water, such that the density of the particle smoothly varies between that of the initial snow aggregate and the final raindrop.

[21] The melting model for spherical particles used in this study is the formulation of *Szyrmer and Zawadzki* [1999] (hereafter SZ99), whereby the energy used to melt snow aggregates is supplied by the ambient environment and the latent heat that is released as water vapor condenses on the particle. With some key assumptions, SZ99 demonstrate the following relation between the energy used per unit time to melt the particle (which is related to the change of melt water), the heat available from the environment, and the heat released as vapor condenses on the particle:

$$L_f \frac{\mathrm{d}m_w}{\mathrm{d}t} = \frac{\mathrm{d}q}{\mathrm{d}t} + L_v \frac{\mathrm{d}m_{cond}}{\mathrm{d}t}, \tag{14}$$

where L_f is the latent heat of fusion, L_v is the latent heat of vaporization, dq is the energy transferred across from the environment to the surface of the particle, and dm_{cond} is the mass of vapor that condenses onto the particle surface. The rate of energy transfer between the environment and the melting particle is a function of the temperature difference δT across the surface of the particle (and thus the environmental lapse rate, Γ_e), the efficiency of heat conduction in the atmosphere, ventilation effects, and the size of the particle. SZ99 demonstrate that

$$\frac{\mathrm{d}m_w}{\mathrm{d}t} = \frac{2\pi B_{fm}}{L_f} \left(K_T \delta T + D_v L_v \delta \rho_v\right) D^{A_{fm}}. \tag{15}$$

where A_{fm} and B_{fm} are parameters determining the ventilation coefficient, K_T is the thermal conductivity of air at 273.15 K, D_v is the water vapor diffusivity in air, and $\delta\rho_v$ is the vapor density difference across the particle calculated from the Clausius-Claperyon equation.

[22] As in SZ99, aggregation or drop breakup are not considered, such that one snowflake melts into one raindrop [e.g., *Du Toit*, 1967; *Ohtake*, 1969]. If the concentration of droplets in the melting and snow phase are given by N_m and N_s, respectively, then this assumption requires the flux of particle number density to be conserved [*Klaassen*, 1988]. Noting that both N and fall speed U are defined in terms of equivalent melted diameter, then for snow, melting particles, and rain,

$$N_s(D)\, U_s(D) = N_m(D)\, U_m(D) = N(D)\, U_r(D), \tag{16}$$

where $N(D)$ is given by equation (5). The fall velocity of rain and snow are taken to follow power law relations,

$$\begin{aligned} U_r(D) &= \alpha_{v,r} D^{\beta_{r,r}} \\ U_s(D) &= \alpha_{v,s} D^{\beta_{r,s}}, \end{aligned} \tag{17}$$

while for melting particles the *Battaglia et al.* [2003] parameterization is used,

$$U_m(D) = \frac{f + f^2}{9.2 - 3.6(f + f^2)} (U_r - U_s) + U_s. \tag{18}$$

[23] Differentiating equation (12) with respect to time and using the chain rule to introduce s as the independent variable,

$$\frac{\mathrm{d}f}{\mathrm{d}s} = \frac{\mathrm{d}f}{\mathrm{d}t} \cdot \frac{\mathrm{d}t}{\mathrm{d}s} = \frac{\mathrm{d}f}{\mathrm{d}t} \cdot \frac{1}{w - U_m}, \tag{19}$$

with w representing the large-scale vertical motion. This variable can be neglected with relatively small error in stratiform rain scenarios, but may be significant in deep convection; ideally, a priori information about w could be used in this calculation. Combining with (15) results in

$$\frac{\mathrm{d}f}{\mathrm{d}s} = -\frac{12\, B_{fm}\, D^{A_{fm}}}{L_f\, \rho_m\, D_m^3\, U_m} \left(K_T \delta T + D_v L_v \delta \rho_v\right). \tag{20}$$

When this equation is integrated over height, one obtains the desired expression for the melted fraction f_j of a particle of melted diameter D, at any height H_j,

$$\begin{aligned} f_j(D, s) &= \int_0^{f_j} \mathrm{d}f \\ &= -\frac{12 B_{fm} D^{A_{fm}}}{L_f} \int_{H_f}^{H_j} \frac{K_T\, \delta T(s) + D_v\, L_v\, \delta \rho_v(s)}{\rho_m(s)\, {D_m}^3(s)\, U_m(s)}\, \mathrm{d}s, \end{aligned} \tag{21}$$

where H_f is the height of the freezing level. Choosing a suitable height increment, approximately 30 m, equation (21) is integrated downward in height for each particle in the distribution, starting with a melted fraction of zero and increasing until the fraction becomes unity. When a particle of a given size is completely melted, it is transferred to the "rain" category. The assumed in-cloud environmental lapse is used to calculate $\delta\ T$ and $\delta\rho_v$.

4.2. Radiative Transfer Model

[24] The formulation of the melting layer model outlined above predicts the melted fraction as a function of height and melted diameter. Although raindrops and highly melted particles may be modeled as spheres, dry snowflakes are highly nonspherical. *Liu* [2004] showed that significant errors are incurred when dry snow flakes are modeled as variable density "soft spheres" at cloud radar frequencies, since non-Rayleigh effects quickly increase with particle size. A better solution is to represent these snowflakes using DDA, whereby complex ice habits can be constructed as a collection of closely spaced dipoles that interact with each other and incident radiation to produce a scattered electric field. At some point, when melting has progressed sufficiently, the particles begin to take on a more spherical form, and a spherical representation containing a mixture of air, ice, and water is appropriate. The transition between these two states is difficult to represent in a physical model, so a hybrid model is adopted that ensures a smooth translation between the optical properties of the snowflake and the partially melted sphere.

[25] First, the optical properties of the partially melted spherical particles are derived. The volume fraction of each species (air, liquid water, ice) must be determined as a function of melted fraction for particles of all sizes. Since

the sum of the volume fractions of air, liquid water, and ice must be unity, it can be easily shown that

$$f_w = \frac{\rho_m}{\rho_w} f$$
$$f_a = \frac{\rho_m \left[1 - \frac{\rho_i}{\rho_m} - f\left(1 - \frac{\rho_i}{\rho_w}\right)\right]}{\rho_a - \rho_i} \tag{22}$$
$$f_i = \frac{\rho_m \left[\frac{\rho_a}{\rho_m} - 1 - f\left(\frac{\rho_a}{\rho_w} - 1\right)\right]}{\rho_a - \rho_i}.$$

The index of refraction of mixed phase hydrometeors follows using a three-component variation on the traditional two-component Bruggeman formulation [*Bruggeman*, 1935; *Johnson*, 2007]. Using this information, the single scattering albedo, extinction, and backscattering coefficients may then be calculated as a function of height for each profile,

$$\begin{bmatrix} k_{sca,o} \\ k_{ext,o} \\ \eta_o \end{bmatrix} = \frac{\pi}{4} \int_0^\infty \begin{bmatrix} Q_{sca}(D) \\ Q_{ext}(D) \\ Q_{sca}(D)\, p_o(\Theta = 180, D) \end{bmatrix} \cdot [N_m(D) + N_c(D) f_{tot}]\, D_m^2 \mathrm{d}D, \tag{23}$$

with the distribution-integrated phase function following as

$$P_o(\Theta) = \frac{\pi}{4\, k_{sca,o}} \int_0^\infty p_o(\Theta, D)\, Q_{sca}(D) \cdot [N_m(D) + N_c(D) f_{tot}]\, D_m \mathrm{d}D. \tag{24}$$

Here Q_{sca} and Q_{ext} are the scattering and extinction efficiencies, respectively, and p_o is the phase function (Θ = 180 indicating the backscatter direction) calculated from Mie theory. In this formulation, the cloud water droplet number concentration has been scaled by the total melted fraction of particles in the distribution,

$$f_{tot} = \frac{\int_0^\infty f \cdot D^3 \, \mathrm{d}D}{\int_0^\infty D^3 \, \mathrm{d}D}. \tag{25}$$

[26] Moving from spheres to more complex ice habits, DDA calculations of the scattering and extinction efficiencies and phase function of snow flakes of various sizes were obtained from the microwave single-scatter property database for nonspherical ice particles constructed by *Liu* [2004]. Individual snowflakes are simulated as aggregates of hexagonal columns. The six-arm bullet rosettes are chosen for this study because they provide reasonable reflectivity and attenuation profiles when integrated over an exponential size distribution (uncertainties due to ice crystal habit are discussed in section 6). The area ratio of the bullets, defined as the ratio of the cross sectional area of the particle to that of a circumscribed sphere with diameter equal to the maximum particle dimension $D_{\max}$, is given by

$$A_r = 0.125\, D_{\max}^{-0.351}, \tag{26}$$

(in cgs units) a relation derived by *Heymsfield and Miloshevich* [2003] on the basis of measurements from the Cloud Particle Imager probe. The DDA database of *Liu* [2004] was used to derive the scatter, extinction, and backscattering coefficients ($k_{ext,d}$, $k_{sca,d}$, η_d) as well as the phase function $P_d(\Theta)$ using equations analogous to (23) and (24).

[27] The equivalent "hybrid" electromagnetic properties can then be evaluated as a mixture of those of a soft sphere and pure snowflake,

$$\begin{bmatrix} k_{ext,m} \\ k_{sca,m} \end{bmatrix} = \zeta \begin{bmatrix} k_{ext,o} \\ k_{sca,o} \end{bmatrix} + (1 - \zeta) \begin{bmatrix} k_{ext,d} \\ k_{sca,d} \end{bmatrix}$$
$$P_m(\Theta) = \frac{1}{k_{sca,m}} \left[\zeta\, k_{sca,o}\, P_o(\Theta) + (1 - \zeta)\, k_{sca,d}\, P_d(\Theta)\right], \tag{27}$$

with

$$\zeta = \begin{cases} f/f_c & , f < f_c \\ 1 & , f \geq f_c \end{cases}, \tag{28}$$

and the backscattering coefficient of the mixture follows as

$$\eta_m = k_{sca,m}\, P_m(\Theta = 180). \tag{29}$$

When the total melted mass fraction reaches f_c, taken to be 0.25 in this study, the particles revert to pure spheres. In this way the electromagnetic properties are nudged toward the DDA values in the initial stages of melting, but revert to spheres containing ice, air, and liquid water as melting progresses.

[28] Now, finally, the radar reflectivity can be calculated as a function of radar range, r. The equivalent radar reflectivity (units of dBZ) is defined as

$$Z_e(r) = 10 \log_{10} \left[\frac{\lambda^4}{\pi^5 |K|^2}\, \eta_m \exp(-A(r)) \times 10^{18}\right], \tag{30}$$

where λ is the radar wavelength, $|K|^2$ is the radar dielectric constant, with the attenuation between the radar and range r given by

$$A(r) = 2 \int_0^r k_{ext,m}(s') \mathrm{d}s'. \tag{31}$$

[29] An example of the melting layer model output is shown in Figure 5 (multiple scattering is included; this is discussed in section 5). Here a 2 mm h^{-1} liquid equivalent precipitation rate was simulated with a lapse rate of 6 K km^{-1}. The thick gray lines show the results with DDA-modeled snowflakes, and the thin solid lines the results for spheres. The radar reflectivity profiles both show a bright band approximately 250 m below cloud top. The spheres-only bright band is more pronounced, primarily because the backscatter efficiency of the volume of DDA-simulated snowflakes at cloud top is higher than that of the melted raindrops at cloud base. It is noted that the presence of a bright band at 94 GHz is often due largely to attenuation effects in the rain below the freezing level, consistent with the findings of *Sassen et al.* [2007].

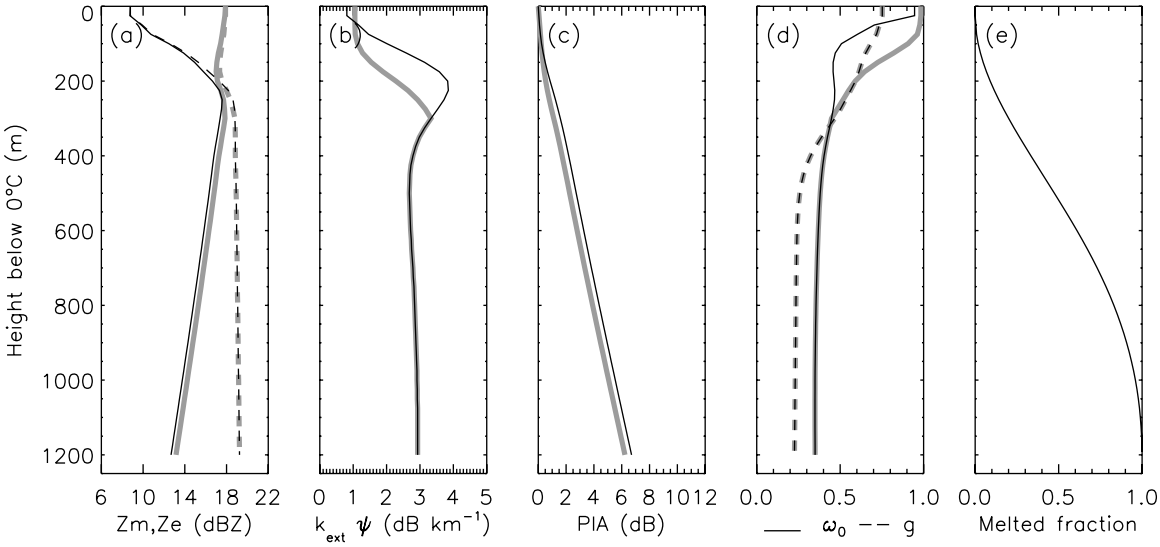

Figure 5. Melting layer model output for a liquid equivalent rain rate of 2 mm h^{-1} with DDA (thick gray lines) and soft spheres (thin black lines). (a) Radar reflectivity, both attenuated (solid line) and unattenuated (dashed line). (b) Attenuation coefficient. (c) PIA. (d) Single scattering albedo (solid line) and asymmetry parameter (dashed line). (e) Melted fraction.

[30] The attenuation profile in both cases peaks near the level of the bright band. The attenuation profile, and thus Z_e, are most uncertain at and just below the freezing level because of uncertainties in ice crystal habit. Once melting has progressed sufficiently, depending partially on the value chosen for f_c, the two methods become nearly identical. PIA, however, is an integrated quantity, and as such the effects of melting near the freezing level propagate downward through the column to the surface. A chief result here is that the presence of a melting layer tends to produce more PIA (through the enhancement just below the melting level) than would result if only warm rain were considered. Therefore, neglecting this additional melting layer contribution to PIA leads to a high bias in retrieved precipitation rate.

5. Multiple Scattering

[31] The Mie solution to particle scattering, as utilized in the rain-only formulation described in section 3, is a single-scatter solution only. Multiple scattering (MS), by contrast, occurs when photons undergo two or more scattering events between the transmitter and receiver. The MS problem is familiar to the lidar community (*Bissonnette* [1988], *Mitrescu* [2005], and others), but has traditionally been less problematic for radar systems. Two chief factors conspire to make MS a factor that cannot be ignored for spaceborne cloud radars like the CPR. First, at W band, scattering by rain and precipitating ice can be significant; the single scattering albedo, ω_0, for rain approaches 0.5, and for snow may be closer to 0.9. The asymmetry parameter, g, which represents the degree of forward scattering, can exceed 0.8 for snow [e.g., *Liu*, 2004; *Skofronick-Jackson et al.*, 2008]. Second, the CPR field of view (FOV) is characterized by a relatively large cross-track footprint (nominally 1.4 km). At W band this is larger than the mean free path of photons in even moderately raining systems, so the probability of more than one scattering event is relatively high.

[32] In heavy precipitation events photons may be scattered several times before arriving at the receiving antenna. This time delay translates into an increase in the apparent range of the source of the scatter. Therefore MS manifests itself as an increase in return power, and thus radar reflectivity, at range gates farther from the radar than the source of the initial scattering event. An indicator of MS in heavy rainfall, often observed by the CPR, is the occurrence of an elevated reflectivity layer that is apparently positioned below the Earth's surface [see *Battaglia et al.*, 2008].

[33] To investigate and quantify the effects of multiple scattering, the CloudSat viewing geometry was incorporated into a backward Monte Carlo modeling of the radiative transfer equation [*O'Brien*, 1992, 1998]. Backward Monte Carlo models conceptually work by firing photons from the receiver antenna and tracing backward, through an absorbing and scattering medium, to the transmitter. Some calculations of received power, P_r, for a homogeneous 4000 m thick raining column are shown in Figure 6. Two examples are shown, one for a rain rate of 1 mm h^{-1} and the other for 5 mm h^{-1}. At 1 mm h^{-1} nearly all the return power is in the first-order scatter (i.e., the backscatter), with the slope of the backscatter power line relating directly to the single-scatter attenuation coefficient. The power returned from second-order scatter is an order of magnitude less than the backscatter, and therefore second-order and higher terms may be neglected. In this case, the traditional radar equation adequately represents the profile of backscattered energy. At 5 mm h^{-1}, however, contributions from higher orders of scatter increase rapidly with depth into the cloud. At cloud base the contribution of terms third order and higher is larger than that from single scatter. Thus it is clear that multiple scattering can only be neglected when rain rates are small, and in practice a value of 3 mm h^{-1} or less is suggested, although more rigorous criteria based on PIA are introduced

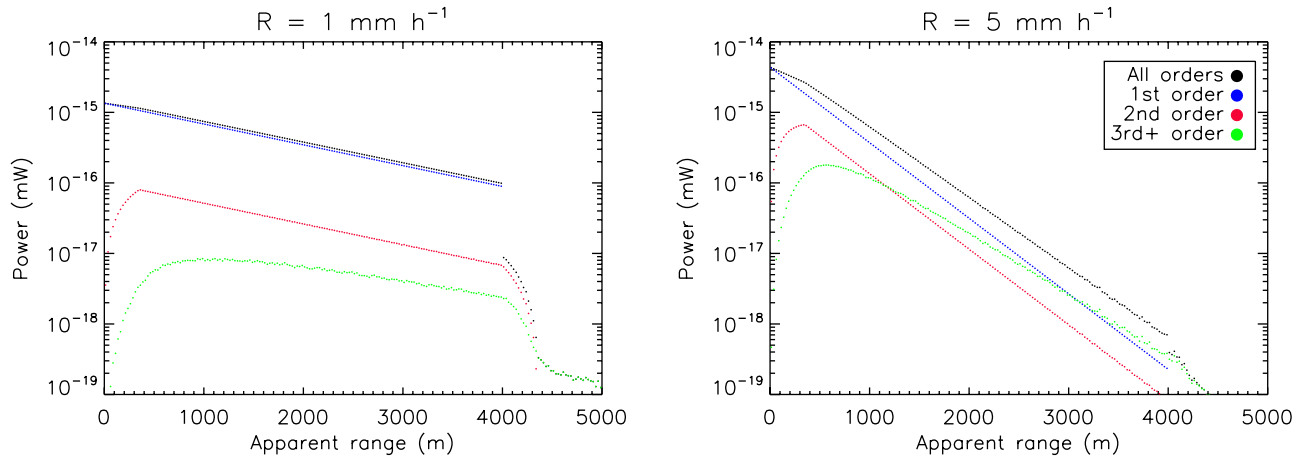

Figure 6. Simulated received power as a function of apparent range for a 4000-m-thick cloud raining at a constant (left) 1 mm h^{-1} and (right) 5 mm h^{-1}, relative to 1 mW transmit power. Color indicates order of scatter.

by *Battaglia et al.* [2008]. In all cases it is noteworthy that MS tends to increase the received power at levels below the precipitation top height, and thus the contribution from MS can also appreciably increase the backscatter from the range bin intersecting the surface. From (2) this indicates that for a given R and raining layer depth, the apparent PIA with MS is smaller than that expected from single-scatter theory only.

[34] The formulation of the full precipitation retrieval algorithm, which includes both melting and multiple scattering effects, requires the creation of a database of received power as a function of depth below cloud top, freezing level height, and environmental lapse rate, for a finite set of cloud depths (0 to 15 km) and rain rates (0.01 to 40 mm h^{-1}). These received powers follow from application of the backward Monte Carlo model, and the power profiles are converted to profiles of attenuated backscattering coefficient, η_{MC}, through the radar equation,

$$\eta_{MC} = \frac{P_r}{P_t} C r^2, \tag{32}$$

where P_t is a reference transmit power, C is a calibration constant determined from boundary conditions at the top of the profile, and r is the range to the target. The corresponding attenuated reflectivity is then

$$Z_{MC} = 10 \log_{10} \left(\frac{\lambda^4}{\pi^5 |K|^2} \eta_{MC} \times 10^{18} \right). \tag{33}$$

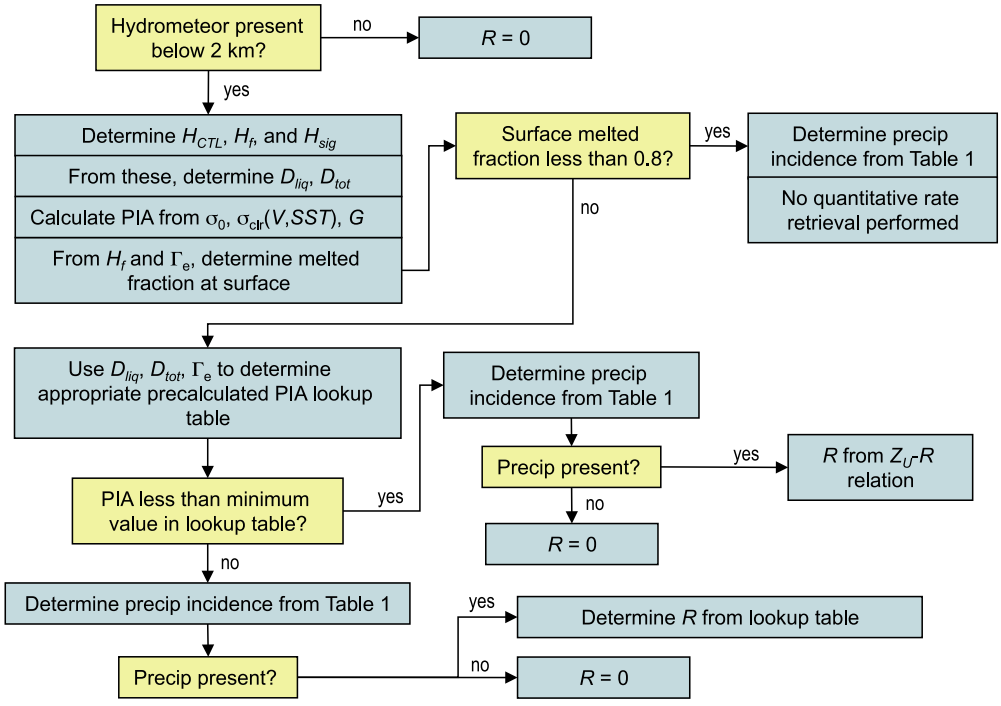

Figure 7. Flowchart for the full rainfall retrieval algorithm.

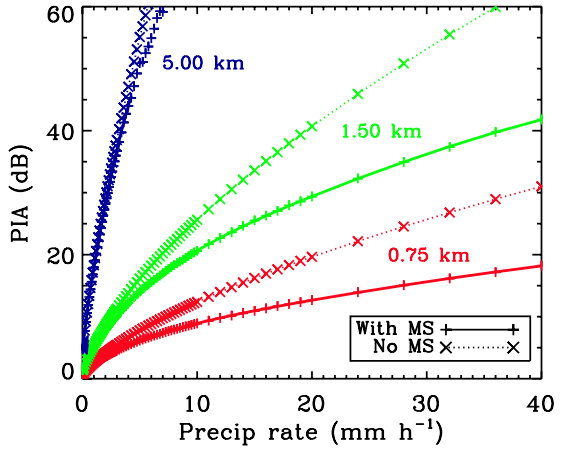

Figure 8. PIA calculated as a function of rain rate for various precipitating layer depths (shown in different colors with the depth value printed adjacent to the corresponding set of lines) with and without multiple scattering.

and the apparent PIA for the profile (i.e., that which includes the effects of multiple scattering) is given by

$$PIA_{app} = Z_e(SFC, A = 0) - Z_{MC}(SFC), \tag{34}$$

where Z_e is the unattenuated reflectivity derived from evaluation of equation (30) with A set to zero, and SFC refers to the level of the surface.

6. Algorithm Formulation and Uncertainties

[35] Following generation of this database, the algorithm can be applied to individual CPR profiles. A flowchart describing the retrieval process is shown in Figure 7. If no hydrometeor is present below 2 km according to the 2B-GEOPROF cloud mask, then R is set to zero. Three critical heights in the radar column are then determined: the lowest layer cloud top (H_{CTL}), the freezing level (H_f), and the height to which frozen particles extend in the atmosphere (H_{sig}). The latter is only considered when a core of significant radar return (>10 dBZ) extends in a continuous column above the freezing level. This is generally only the case in convective cores, and represents less than 6% of CloudSat retrievals.

[36] From these critical heights, each profile is classified according to the depth of the liquid/mixed layer, D_{liq}, the total depth of the precipitating layer, D_{tot}, and the assumed environmental lapse rate, Γ_e. If only warm rain is possible, then $D_{liq} = D_{tot} = H_{CTL}$. When a cloud column extends above the freezing level, but no significant reflectivity core is present as described above, then $D_{liq} = D_{tot} = H_f$, and hydrometeors are considered to start as snow at the freezing level and melt into rain. When a significant reflectivity core is present, then $D_{liq} = H_f$ and $D_{tot} = H_{sig}$. In this case, precipitation starts as snow and begins melting into rain at the freezing level.

[37] The PIA associated with the profile is calculated as described in section 2. Next, the melted fraction is determined as a function of height below the freezing level using the melting layer model initialized with the assumed lapse rate. When the melted fraction at the surface is less than 0.8, no quantitative retrieval is performed. This criterion is enforced to limit uncertainties associated with mixed phase precipitation and algorithm uncertainties are largest when the freezing level is low (discussed later in this section). The occurrence of precipitation may still be determined, however, using the unattenuated near-surface reflectivity (equation (9) and Table 2).

[38] For profiles with surface melted fraction ≥ 0.8, the appropriate precalculated lookup table is determined from the three critical heights associated with the profile. If the observed PIA is less than the smallest value in the table (i.e., that associated with cloud only) then precipitation occurrence is again obtained from the unattenuated near-surface reflectivity. R is obtained directly from Z_u using a separate lookup table of Mie-generated reflectivities and rain rates. This table is created from the rain and cloud DSDs given by (5) and (6). Rain rates obtained from these cases with very small PIA rarely exceeds 0.5 mm h^{-1}. In most cases, the observed PIA is larger than the minimum contained in the table. In these cases R is retrieved by matching the observed PIA to the precalculated values of apparent PIA.

[39] Some examples of calculated PIA versus rain rate relations for warm rain only, with and without multiple scattering effects, are shown in Figure 8. It is apparent that for very light rain, MS has a negligible contribution to PIA. Above a few millimeters per hour, however, the MS contribution can be significant. For example, consider a 0.75 km deep raining layer with an observed PIA of 15 dB; the retrieved rain rate without MS is approximately 13 mm h^{-1}; with MS it is 28 mm h^{-1}. Since MS adds energy to the surface return, the apparent PIA required to achieve the same rain rate is reduced when properly accounting for MS; failure to account for MS biases retrieved rain rates low.

[40] As discussed earlier, at W band, precipitating ice has both a high single scattering albedo and asymmetry parameter (Figure 5), and as a result significant MS can occur. MS tends to "turn on" quickly above a threshold precipitation rate, as demonstrated also by *Battaglia et al.* [2006]. Figure 9

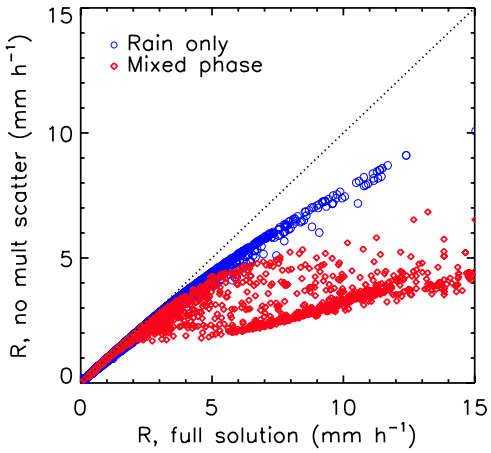

Figure 9. One day of CloudSat-based precipitation retrievals. Blue points contain only warm rain, and red points contain a mixture of precipitating ice, melting particles, and possibly rain.

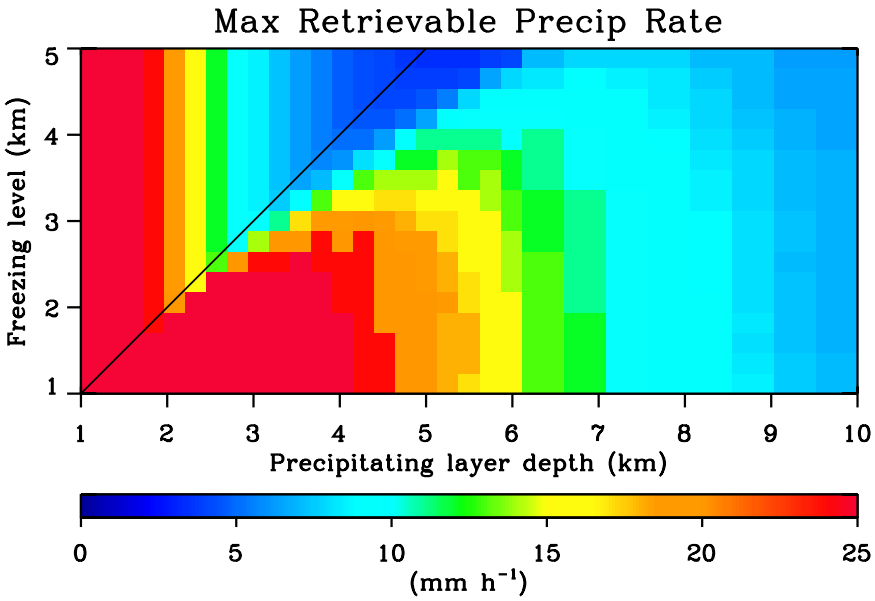

Figure 10. Maximum retrievable precipitation rate, estimated using a conservative 40-dB PIA cutoff for applicability of SRT methods.

shows precipitation retrievals for one day of CloudSat orbits. The blue points indicate retrievals with only warm rain, and the red points are retrievals containing a mix of precipitating ice, melting particles, and possible rain. The tendency to underestimate R without properly accounting for MS is demonstrated by the departure of the blue points from the one-to-one line. The rapid turn-on of ice phase scattering at approximately 2–3 mm h^{-1} and large departures from single-scatter theory are also apparent.

[41] Combining the effects of attenuation, MS, and particle melting together, one can estimate the maximum retrievable precipitation rate (MRP) for the CPR using this method. Although the CPR is capable of detecting more than 50 dB of two-way attenuation, *Battaglia et al.* [2008] suggest a cutoff of approximately 40 dB for the applicability of surface reflectance technique (SRT) methods such as the present retrieval. It is argued that when PIA exceeds this threshold, MS in the atmosphere is so significant that it potentially masks scattering from the surface itself. Thus, using this 40 dB threshold, a conservative estimate of the MRP may be obtained as a function of precipitating layer depth and freezing level height (Figure 10). For warm rain (points above the one-to-one line), MRP is a function of precipitating layer depth only; while it is possible to retrieve 25 mm h^{-1} or greater for a 1 km deep system, this reduces to about 7 mm h^{-1} for a 4 km deep system. When melting effects are considered, MRP increases since MS by ice and melting particles tends to increase return power from the surface (whereas attenuation acts to decrease it).

[42] When making deductions about a physical quantity by applying measurements to a forward model, it is important to quantify the sensitivity of the model to the measurements, input parameters, and various assumptions, as well as the measurement uncertainties of the instrument. To this end an uncertainty analysis is performed. Seven parameters are considered as chief contributors to uncertainty in precipitation rate using this method: the cloud to rain water ratio, the drop size distribution, the environmental lapse rate, the slope of the rain profile, the shape of ice crystals, the height of the freezing level, and the uncertainty in measured PIA. To test the influence of these parameters on retrieved precipitation rates, the retrieval is run multiple times on two full weeks of near-global CloudSat observations, each time perturbing one of these parameters by an amount sufficient to capture the uncertainty in the parameter. Retrievals where the MRP is encountered are discarded from this analysis. Considering a system of p-independent parameters such that covariances may be neglected, the total fractional uncertainty in retrieved precipitation rate, ϵ, is given by the square root of the sum of the squares of the fractional uncertainty in each parameter,

$$\epsilon_{i,j} = \sqrt{\sum_{k=1}^{p} \left[\left(\frac{\overline{\delta R_k}}{R_{i,j}} \right)^2 \right]}. \tag{35}$$

Here the uncertainties are broken down into 25 precipitation rate bins between 0 and 25 mm h^{-1}, and 8 freezing level height bins between 1 and 5 km, with bin numbers represented by the i and j subscripts (Figure 11). It should be noted that this analysis assumes that individual sources of error are uncorrelated and therefore provides an upper bound on the combined total uncertainty in the retrieval. The absence of concrete estimates of the magnitude of correlations among these various sources of error precludes us from further refining the expected retrieval uncertainty at this time.

[43] To assess the influence of the ratio of assumed cloud to rain water content, the ratio is varied by a factor of 2 in both the positive and negative directions. This ratio reflects uncertainty in whether attenuation is due to cloud drops or precipitation drops, and also the inherent ambiguity between the two during the incipient stages of precipitation formation. Since the ratio is largest for small R, it is not

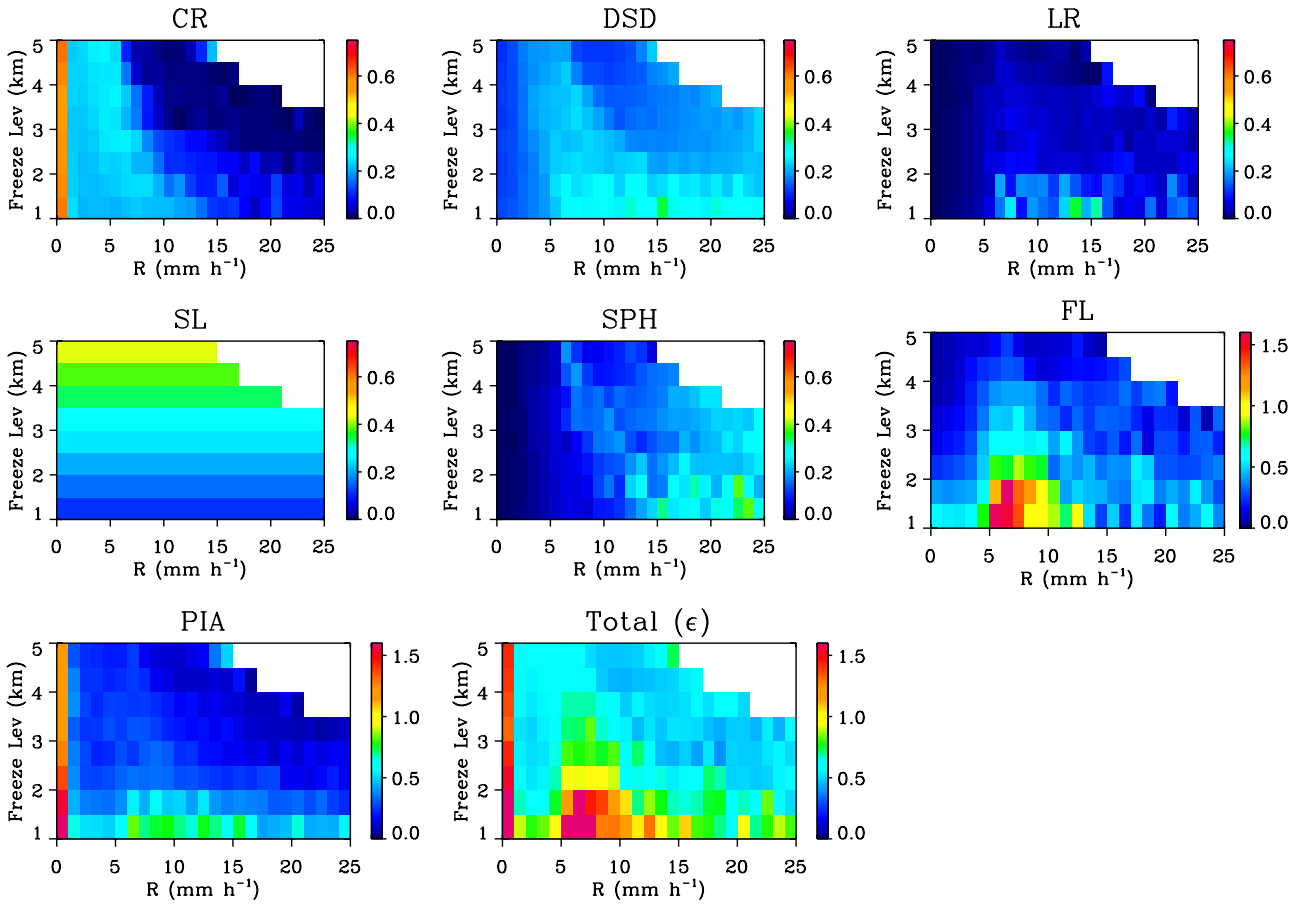

Figure 11. Fractional uncertainty in retrieved precipitation rate due to each of seven parameters (CR, cloud to rain water ratio; DSD, drop size distribution; LR, environmental lapse rate; SL, rainfall slope; SPH, sphere versus bullet rosette ice crystal habit; FL, freezing level height; PIA, measured path-integrated attenuation) as a function of precipitation rate and freezing level height. Total fractional uncertainty due to uncertainty in these parameters is shown in the last panel.

surprising that the fractional uncertainty is largest (about 0.6) for $R < 0.1$ mm h^{-1}, but drops off quickly as R increases.

[44] To test the effects of DSD, two different modified gamma distributions of precipitation drops of the form used in the TRMM PR 2A25 algorithm are substituted for the assumed Marshall-Palmer distribution,

$$N(D) = N_\Gamma D^\mu \exp\left(-\left[\frac{3.67+\mu}{D_\Gamma}\right] D\right), \qquad (36)$$

with μ taken the be 3. The values of N_Γ and D_Γ are derived as a function of R from the TRMM stratiform and convective power law relations between radar reflectivity and rain rate [*Iguchi et al.*, 2000] as well as the raindrop fall velocity relations described in section 4. Resulting fractional uncertainties in R are generally less than 0.3, being largest for moderate rain rates at low freezing levels. The magnitude of these uncertainties is consistent with the findings of *Matrosov* [2007], who estimated DSD-related uncertainties in rain rate from a PIA-based method based on observed DSDs. Perturbing the environmental lapse rate by 1 K km^{-1} each direction is shown to have a smaller overall effect than perturbing the DSD, but the effects are concentrated in similar regimes.

[45] The retrieval algorithm assumes a constant rainfall profile below the freezing level, as described in section 3. To assess errors in retrieved rain rate produced by rain profiles that vary with height, sets of rain profiles are constructed that vary linearly between the surface and the freezing level. The slope of these profiles, normalized by the mean rain rate, is taken to vary between -0.15 km^{-1} and 0.03 km^{-1}, with a negative slope indicating rain rate increasing toward the surface. These representative slopes are based on the work of *Fu and Liu* [2001] who analyzed the shape of precipitation profiles observed by the TRMM PR. They found that although stratiform rain profiles are generally height invariant below the freezing level, convective rainfall may either increase or decrease between the freezing level and the surface. Applying these perturbed rain profiles to the current algorithm is found to produce uncertainties that are very small compared with the inherent uncertainty arising because the surface rain rate may vary considerably from the column mean; it is these errors that are reflected in the fourth panel of Figure 11. The fractional uncertainty is shown to vary between approximately 0.1 and 0.6, with the largest errors associated with the highest freezing levels. It is noteworthy that the retrieval is likely to perform best for stratiform-type rain not only because precipitation is more likely to be height invariant, but also

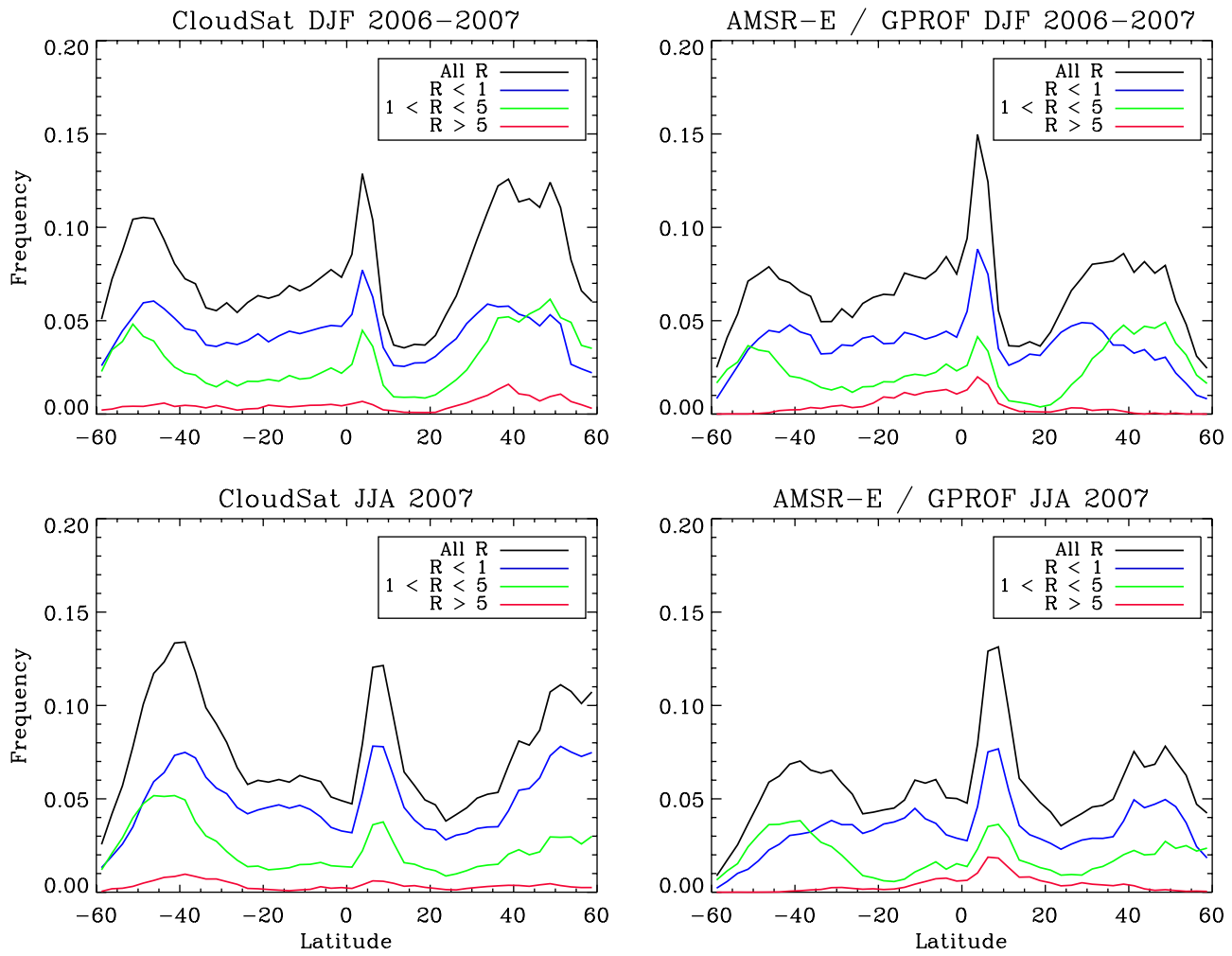

Figure 12. Frequency of occurrence of oceanic liquid precipitation. Rain rate categories are indicated by colors; (left) CloudSat rain rates are averaged to the footprint size of (right) AMSR-E for (top) DJF 2006–2007 and (bottom) JJA 2007.

because convective precipitation often features graupel, supercooled water that has been lofted above the melting level, and higher, less uniform vertical velocities.

[46] Retrieval uncertainties due to choice of ice crystal habit are difficult to quantify. Offline calculations of radar reflectivity and attenuation were produced using the *Liu* [2004] database for a variety of habits, including six-arm bullet rosettes, sector plates, hexagonal plates, columns, and spheres. Since precipitating ice crystals often have irregular shapes [*Mogono*, 1953; *Heymsfield et al.*, 2002, 2004], plates and columns are not particularly representative of snowfall distributions. Of the remaining species, the largest differences in reflectivity and attenuation were between bullet rosettes and spheres, so the retrieval was run with spheres only and then with bullet rosettes, and uncertainties calculated from these results. Fractional uncertainties associated with ice crystal habit generally increase with R, but rarely exceed 0.2 for $R < 10$ mm h^{-1}.

[47] Uncertainties due to specification of the freezing level are a function of uncertainty in the ECMWF temperature. Assuming a 0.73 K uncertainty in temperature at 700 hPa [*Eyre et al.*, 1993] and an environmental lapse rate of 6 K km^{-1}, this translates to a height uncertainty of approximately 125 m. This value is quadrupled to account for the fact that precipitation, especially in the middle latitudes, can occur in regions of large temperature gradients, and these gradients may not be resolved by the model; therefore, a 250 m perturbation in freezing level height is employed in both directions. The resulting uncertainties are greatest for low freezing level heights, since R is most sensitive to PIA when precipitation layer depth is small. When the freezing level is low and R is between 5 and 10 mm h^{-1}, the fractional uncertainty approaches 2. This is because multiple scattering by ice in this regime tends to partially compensate for attenuation effects in the rain below [see *Battaglia et al.*, 2006], producing a regime where apparent PIA is nearly invariant over a range of R.

[48] Finally, uncertainties in the measured PIA are assessed by perturbing these measurements by one standard deviation, the value of which depends on wind speed (see section 2). The resulting uncertainties are largest for small R, and again for lower freezing level heights. The resulting total fractional uncertainties due to uncertainties in these seven parameters are shown in the last panel of Figure 11.

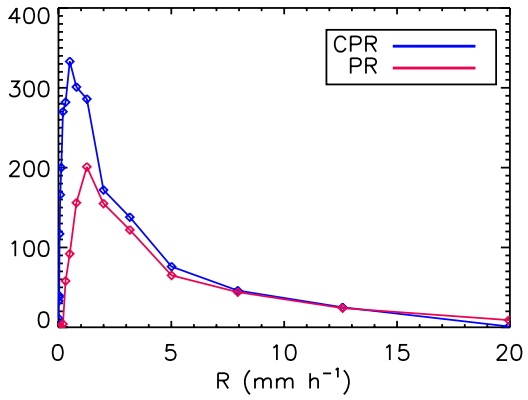

Figure 13. Histogram of frequency of occurrence of precipitation viewed by the TRMM PR and CPR for all crossover matches between 30° south and 30° north latitude, during the period from June 2006 to November 2007. Bin size increases with R, as shown by the diamonds.

As expected, there are two regimes where fractional uncertainty in retrieved R can be expected to exceed 1: when the precipitation rate is less than about 0.5 mm h^{-1}, and when the freezing level is below 2 km and the precipitation rate is between approximately 5 and 10 mm h^{-1}. In practice, uncertainties are expected to be largest in the middle and higher latitudes in storm systems with moderate precipitation.

7. Results

[49] The full algorithm is applied to CloudSat data to produce near-global precipitation distributions. These results are also compared with other data sets. One such comparison is made against passive microwave precipitation estimates from AMSR-E, utilizing the Goddard Profiling Algorithm (GPROF) [*Kummerow et al.*, 2001]. AMSR-E passes over any given scene approximately 1 minute before it is viewed by the CPR. It is noted that the CloudSat footprint is considerably smaller than the 14 by 8 km footprint of the 36.5 GHz channel of AMSR-E, such that there may be considerable variability captured by the CPR within the AMSR-E FOV.

[50] Figure 12 shows the zonal mean occurrence of liquid precipitation (the "rain definite" category of Table 2) as observed by CloudSat for December through February 2006–2007 (DJF) and June through August 2007 (JJA). Each panel of Figure 12 suggests a trimodal latitudinal structure of precipitation occurrence, with peaks in the intertropical convergence zone (ITCZ) and both the northern and southern midlatitude storm tracks. Total precipitation occurrence from the CPR compares well with AMSR-E in the tropics and subtropics. The colored lines of Figure 12 show occurrence categorized by rain rate (here the CPR rain rates have been averaged over the footprint size of AMSR-E). Considerable differences in occurrence are present in higher latitudes, where the CPR observes precipitation nearly twice as often as AMSR-E in some latitude bands. These differences are particularly pronounced in region of the southern hemisphere winter storm tracks. These high-latitude differences are not unexpected since the GPROF cloud property database that forms the basis of the AMSR-E rain retrieval is tuned to tropical cloud systems. More results on the frequency of occurrence of precipitation observed by CloudSat, particularly in relation to the types of cloud systems present, are given by *Haynes and Stephens* [2007].

[51] The full retrieval algorithm is also compared against direct matches with TRMM PR overpasses. Although TRMM flies in a lower altitude, lower inclination orbit that the A-Train, crossovers occur approximately twice per day. A crossover match is considered to be any oceanic observation where the center of the TRMM and CPR footprint fall within 3.5 km and 5 minutes of each other. Since the nadir footprint of the PR, about 5 km, is larger than the CPR footprint, up to seven overlapping CPR precipitation rates must be averaged together for comparison with a single PR precipitation rate. The period from June 2006 to November 2007 was scanned for crossover matches in the tropical region between 30° south and 30° north latitude, resulting in approximately 30,000 independent PR footprints where either PR or CPR observed rain.

[52] A histogram of precipitation rates resulting from these crossover matches is shown in Figure 13. First, it is noted that the CPR observes more rain than the PR, particularly for $R < 2$ mm h^{-1}. The CPR peak occurs at about 0.5 mm h^{-1} whereas the PR peak is closer to 1.3 mm h^{-1}. This is an expected consequence of the higher sensitivity of the CPR. Second, for higher precipitation rates, the counts are comparable. The PR observes more rainfall in excess of approximately 12 mm h^{-1} than the CPR, which is also expected given the aforementioned limitations of attenuation-based methods at millimeter wavelengths.

[53] An example crossover match from the central Pacific on 1 December 2006 is shown in Figure 14. The CPR is sensitive to both clouds and precipitation, so the area of detectable reflectivity covers a much larger area than what is observed by the PR. In this example the CPR detects precipitation (particularly less than 1–2 mm h^{-1}) more often than the PR, consistent with the aggregated statistics shown in Figure 13. The period between 34.7 and 35.2° latitude is notable and illustrates this point; here the PR detects no significant reflectivity, but the CPR observes constant light precipitation falling through a bright band feature near 4.5 km. There are also periods when the PR retrieves heavier precipitation than the CPR, such as near 33.9° latitude. In this case the CPR beam is significantly (but not completely) attenuated. It should be noted that individual retrievals may differ for reasons other than the methodology utilized, including differences due to the time and distance parameters that define a match, spatial translation of the precipitation systems, and footprint differences between the two sensors.

[54] Finally, Figure 15a shows the accumulated water mass as a function of latitude derived from the CPR and a variety of other data sets during the DJF 2006–2007 season (now presented at their native resolutions with no "matching" performed). In addition to AMSR-E and the TRMM PR, data from the TRMM Microwave Imager (TMI) and the Global Precipitation Climatology Project (GPCP) are also displayed. GPCP combines precipitation observations from a variety of sources aiming to formulate a climatological "best estimate" of accumulated global rainfall [*Adler et al.*, 2003]. Although sampling differences between instruments must always be considered in such comparisons, errors introduced by the diurnal sampling characteristics of

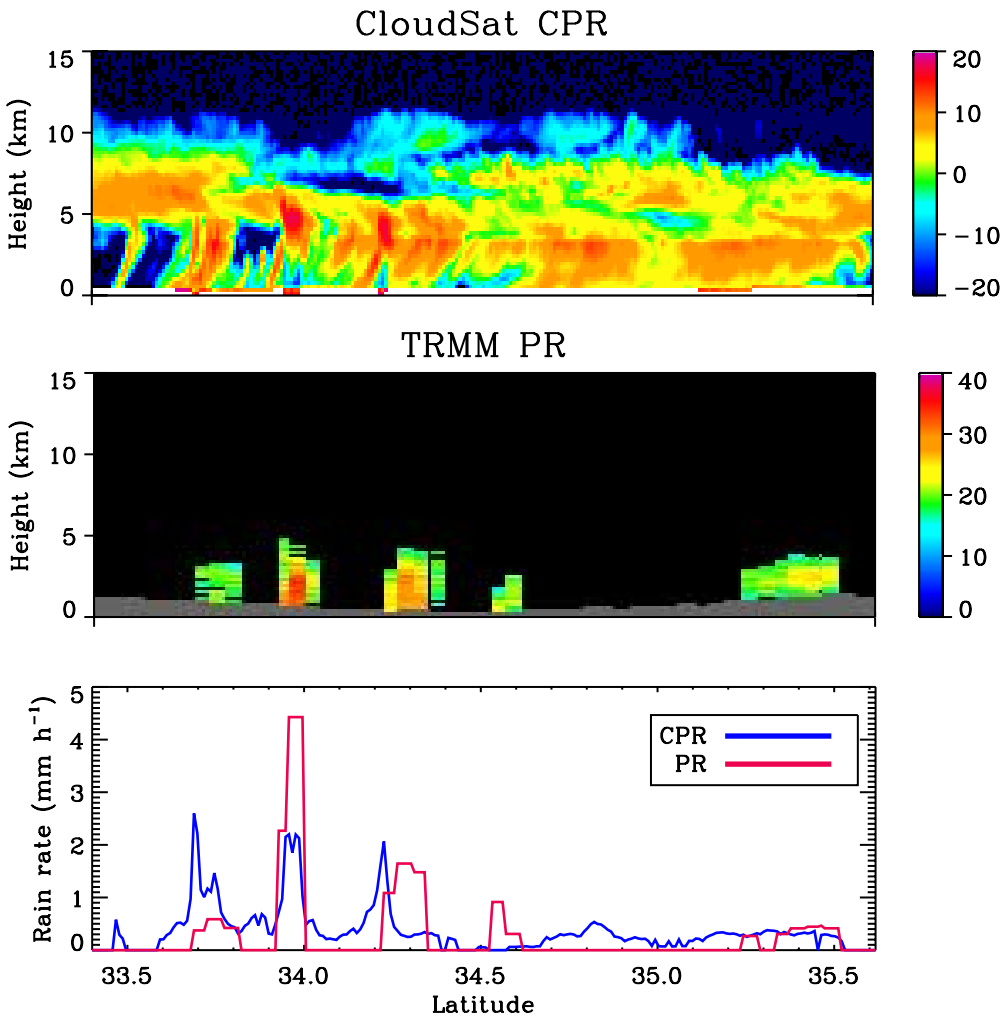

Figure 14. (top) CPR reflectivity (dBZ), (middle) PR reflectivity (dBZ), and (bottom) rain rate retrievals for a 1 December 2006 crossover match.

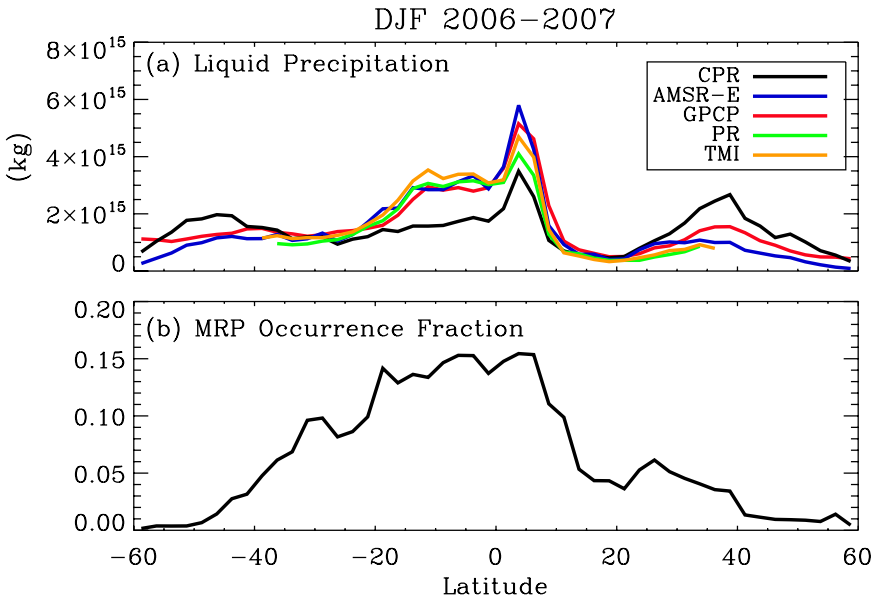

Figure 15. (a) Liquid precipitation accumulation over the global oceans as a function of latitude. Accumulations are weighted by the ocean area of each 2.5° latitude bin. (b) Fraction of raining retrievals where the maximum retrievable precipitation rate is encountered.

CloudSat are probably small compared with the magnitude of the differences in Figure 15a. *Nesbitt and Zipster* [2003] estimated that rainfall over the tropical oceans exhibits a diurnal cycle that varies by approximately 30%, maximum the in the predawn hours with a late afternoon minimum. CloudSat samples the tropical atmosphere approximately 4 hours prior to either of these extremes, reducing the temporal sampling bias to less than 5% utilizing the Nesbitt and Zipster results.

[55] Some differences between CPR rainfall and that derived from other sensors are apparent. A dual-peaked ITCZ is present in most of the data sets between −20° S and 5° N latitude. The CPR rainfall estimates in this region, however, are relatively low. The reason lies in the high frequency with which the maximum retrievable precipitation rate is encountered in the tropics (Figure 15b). More frequent intense rainfall leads to more frequent saturation of the surface backscatter signal. When this occurs the retrieval algorithm is unable to quantify how intense the rainfall is beyond the MRP. While the CPR retrieval performs best at the lower end of the rainfall intensity spectrum, sensors like the PR are well suited to observe heavy rain. The synergy of combining the different types of information provided by these two instruments is again emphasized.

[56] Transitioning into the middle latitude storm tracks, however, there is considerable variance between all estimates. CPR accumulated rainfall is considerably higher than both passive microwave and PR estimates. The source of these differences is not known, but some speculation is possible. As discussed earlier in this section, performance of the full retrieval algorithm becomes more uncertain as the freezing level lowers to 1–2 km, particularly for precipitation rates between 5 and 10 mm h^{-1}, and retrieval analysis (not shown) shows that the bulk of this precipitation occurs from cases where $R > 5$ mm h^{-1}. Therefore CloudSat estimates may be biased high. It is also known, however, that microwave precipitation estimates based on GPROF (AMSR-E and TMI) are degraded when applied outside the tropics. Unfortunately it is difficult to validate rainfall retrievals (and the effects of omnipresent uncertainties such as DSD) over the middle latitude oceans since virtually no regular in situ measurements of rainfall exist. It is noteworthy, however, that these uncertainties in mass of accumulated water are unrelated to the finding that the CPR observes precipitation significantly more often over the middle-latitude oceans, particularly during the winter season, than is indicated by passive microwave measurements. This is consistent with the findings of *Petty* [1997], who compared passive microwave precipitation estimates over the ocean with shipboard observations and concluded that, poleward of about 45°, the surface observations showed a significantly higher frequency of precipitation occurrence than the satellite estimates.

8. Conclusions

[57] W-band radars such as the CloudSat CPR are sensitive to both clouds and precipitation, and are particularly well suited to the discrimination of raining clouds from nonraining clouds, as well as the quantification of light to moderate precipitation. For this purpose, attenuation by hydrometeors is an advantage of W-band radars, because the magnitude of this attenuation is related to the intensity of precipitation in the atmospheric column observed by the radar. By measuring the strength of backscatter from the ocean surface and the low-level radar reflectivity, it is possible to determine, with high confidence, whether precipitation is occurring within the radar footprint. It has also been demonstrated that the radar is sensitive to precipitation rate, within the limits of saturation. Multiple scattering effects are significant for precipitation more intense than approximately 3 mm h^{-1}, and melting particle effects may also be important when precipitating ice is present. Failure to account for either of these processes results in biases in retrieved precipitation rates.

[58] Seasonal retrieval statistics suggest that a greater amount of rain falls over the middle- and high-latitude oceans than has previously been detected using passive microwave techniques. It is difficult to verify these retrievals, however, owing to lack of in situ rainfall measurements over high-latitude oceans. Validation campaigns will be essential to verify the amount of rain that falls in storm tracks and establish a baseline for comparison.

[59] Finally, it is notable that CloudSat is the first active, spaceborne observing system to regularly quantify rain outside the subtropics. It has been demonstrated that the CPR detects light rainfall more often than the TRMM Precipitation Radar, owing primarily to the operating frequency and higher sensitivity of the CPR. The PR, in turn, quantifies heavier rain that is beyond the measurement capabilities of the CPR. This is one example of the synergy resulting from the combination of CloudSat observations with other precipitation sensors; this combination has great potential to provide new information about how precipitation is distributed on our planet.

[60] **Acknowledgments.** This study was supported partially by NASA grant NNX07AR97G. We wish to thank Denis O' Brien of Colorado State University for providing the backward Monte Carlo model used in this study and for his assistance adapting it for use in the CloudSat configuration. Simone Tanelli's contribution was performed at the Jet Propulsion Laboratory, California Institute of technology, under contract with the National Aeronautics and Space Administration.

References

Adler, R. F., et al. (2003), The version-2 Global Precipitation Climatology Project (GPCP) monthly precipitation analysis (1979–Present), *J. Hydrometeorol.*, *4*, 1147–1167.

Austin, R. T., and G. L. Stephens (2001), Retrieval of stratus cloud microphysical parameters using millimeter-wave radar and visible optical depth in preparation of CloudSat: 1. Algorithm formulation, *J. Geophys. Res.*, *106*, 28,233–28,242.

Battaglia, A., C. Kummerow, D. Shin, and C. Williams (2003), Constraining microwave brightness temperatures by radar brightband observations, *J. Atmos. Oceanic Technol.*, *20*, 856–871.

Battaglia, A., M. O. Ajewole, and C. Simmer (2006), Evaluation of radar multiple scattering effects in CloudSat configuration, *Atmos. Chem. Phys.*, *7*, 1719–1730.

Battaglia, A., J. M. Haynes, T. L'Ecuyer, and C. Simmer (2008), Identifying multiple-scattering-affected profiles in CloudSat observations over the oceans, *J. Geophys. Res.*, *113*, D00A17, doi:10.1029/2008JD009960.

Bissonnette, L. R. (1988), Multiple scattering of narrow light beams in aerosols, *Appl. Opt.*, *27*, 2478–2484.

Bohren, C. F., and D. R. Huffman (1983), *Absorption and Scattering of Light by Small Particles*, 530 pp., John Wiley, Hoboken, N. J.

Bruggeman, D. A. G. (1935), Berechnung verschiedener physikalischer Konstanten von heterogenen Substanzen, *Ann. Phys.*, *24*, 636–679.

Du Toit, P. S. (1967), Doppler radar observations of drop size in continuous rain, *J. Appl. Meteorol.*, *6*, 1082–1087.

Eyre, J. R., G. A. Kelly, A. P. McNally, E. Andersson, and A. Persson (1993), Assimilation of TOVS radiances information through one-dimensional variational analysis, *Q. J. R. Meteorol. Soc.*, *119*, 1427–1463.

Fabry, F., and I. Zawadzki (1995), Long-term radar observations of the melting layer of precipitation and their interpretation, *J. Atmos. Sci.*, *52*, 838–851.

Freilich, M. H., and B. A. Vanhoff (2003), The relationship between winds, surface roughness, and radar backscatter at low incidence angles from TRMM precipitation radar measurements, *J. Atmos. Oceanic Technol.*, *20*, 549–562.

Fu, Y., and G. Liu (2001), The variability of tropical precipitation profiles and its impact on microwave brightness temperatures as inferred from TRMM data, *J. App. Meteorol.*, *40*, 2130–2143.

Hardaker, P. J., A. R. Holt, and C. G. Collier (1995), A melting-layer model and its use in correcting for the bright-band in single-polarization radar echoes, *Q. J. R. Meteorol. Soc.*, *121*, 495–525.

Haynes, J. M., and G. L. Stephens (2007), Tropical oceanic cloudiness and the incidence of precipitation: Early results from CloudSat, *Geophys. Res. Lett.*, *34*, L09811, doi:10.1029/2007GL029335.

Heymsfield, A. J., and L. M. Miloshevich (2003), Parameterizations for the cross-sectional area and extinction of cirrus and stratiform ice particles, *J. Atmos. Sci.*, *60*, 936–956.

Heymsfield, A. J., A. Bansemer, P. R. Field, S. L. Durden, J. L. Stith, J. E. Dye, W. Hall, and C. A. Grainger (2002), Observations and parameterizations of particle size distributions in deep tropical cirrus and stratiform precipitating clouds: Results from in situ observations in TRMM field campaigns, *J. Atmos. Sci.*, *59*, 3457–3491.

Heymsfield, A. J., A. Bansemer, C. Schmitt, C. Twohy, and M. R. Poellot (2004), Effective ice particle densities derived from aircraft data, *J. Atmos. Sci.*, *61*, 982–1003.

Iguchi, T., T. Kozu, R. Meneghini, J. Awaka, and K. Okamoto (2000), Rain-profiling algorithm for the TRMM precipitation radar, *J. Appl. Meteorol.*, *39*, 2053–2070.

Johnson, B. (2007), Multi-frequency passive microwave and dual-frequency radar remote sensing of snowfall, Ph.D. dissertation, Univ. of Wisconsin-Madison, Madison.

Klaassen, W. (1988), Radar observations and simulation of the melting layer of precipitation, *J. Atmos. Sci.*, *45*, 3741–3753.

Kummerow, C., Y. Hong, W. S. Olson, S. Yang, R. F. Adler, J. McCollum, R. Ferraro, G. Petty, D. B. Shin, and T. T. Wilheit (2001), The evolution of the Goddard Profiling Algorithm (GPROF) for rainfall estimation from passive microwave sensors, –it, *J. Appl. Meteorol.*, *40*, 1801–1820.

L'Ecuyer, T. S., and G. L. Stephens (2002), An estimation-based precipitation retrieval algorithm for attenuating radars, *J. Appl. Meteorol.*, *41*, 272–285.

Li, L., G. M. Heymsfield, L. Tian, and P. E. Racette (2005), Measurements of ocean surface backscattering using an airborne 94-GHz cloud radar—Implication for calibration of airborne and spaceborne W-Band radars, *J. Atmos. Oceanic Technol.*, *22*, 1033–1045.

Liebe, H. J. (1985), An updated model for millimeter wave propagation in moist air, *Radio Sci.*, *20*, 1069–1089.

Liu, G. (2004), Approximation of single scattering properties of ice and snow particles for high microwave frequencies, *J. Atmos. Sci.*, *61*, 2441–2456.

Marshall, J. S., and W. M. Palmer (1948), The distribution of raindrops with size, *J. Meteorol.*, *5*, 165–166.

Matrosov, S. Y. (2007), Potential for attenuation-based estimations of rainfall rate from CloudSat, *Geophys. Res. Lett.*, *34*, L05817, doi:10.1029/2006GL029161.

Miles, N. L., J. Verlinde, and E. E. Clothiaux (2000), Cloud droplet size distributions in low-level stratiform clouds, *J. Atmos. Sci.*, *57*, 295–311.

Mitrescu, C. (2005), Lidar model with parameterized multiple scattering for retrieving cloud optical properties, *J. Quant. Spectrosc. Radiat. Transfer*, *94*, 201–224.

Mogono, C. (1953), On the growth of snow flake and graupel, Sci. Rep. 2, pp. 18–40, Yokohama Natl. Univ., Yokohama, Japan.

Nesbitt, S. W., and E. J. Zipster (2003), The diurnal cycle of rainfall and convective intensity according to three years of TRMM measurements, *J. Clim.*, *16*, 1456–1475.

O'Brien, D. M. (1992), Accelerated quasi Monte Carlo integration of the radiative transfer equation, *J. Quant. Spectrosc. Radiat. Transfer*, *48*, 41–59.

O'Brien, D. M. (1998), Monte Carlo integration of the radiative transfer equation in a scattering medium with stochastic reflecting boundary, *J. Quant. Spectrosc. Radiat. Transfer*, *60*, 573–583.

Ohtake, T. (1969), Observations of the size distribution of hydrometeors through the melting layer, *J. Atmos. Sci.*, *26*, 545–557.

Petty, G. W. (1997), An intercomparison of oceanic precipitation frequencies from 10 special sensor microwave/imager rain rate algorithms and shipboard present weather reports, *J. Geophys. Res.*, *102*, 1757–1777.

Platnick, S., M. D. King, S. A. Ackerman, W. P. Menzel, B. A. Baum, J. C. Riedi, and R. A. Frey (2003), The MODIS cloud products: Algorithms and examples from Terra, *IEEE Trans. Geosci. Remote Sens.*, *41*, 459–473.

Sassen, K., S. Matrosov, and J. Campbell (2007), CloudSat spaceborne 94 GHz radar bright bands in the melting layer: An attenuation-driven upside-down lidar analog, *Geophys. Res. Lett.*, *34*, L16818, doi:10.1029/2007GL030291.

Skofronick-Jackson, G., A. Heymsfield, E. Holthaus, C. Albers, and M.-J. Kim (2008), Nonspherical and spherical characterization of ice in Hurricane Erin for wideband passive microwave comparisons, *J. Geophys. Res.*, *113*, D06201, doi:10.1029/2007JD008866.

Stephens, G. L., and J. M. Haynes (2007), Near global observations of the warm rain coalescence process, *Geophys. Res. Lett.*, *34*, L20805, doi:10.1029/2007GL030259.

Stephens, G. L., and N. B. Wood (2007), Properties of tropical convection observed by millimeter-wave radar systems, *Mon. Weather Rev.*, *135*, 821–842.

Stephens, G. L., et al. (2002), The Cloudsat mission and the A-Train, *Bull. Am. Meteorol. Soc.*, *83*, 1771–1790.

Stephens, G. L., et al. (2008), The CloudSat mission: Performance and early science after the first year of operation, *J. Geophys. Res.*, *113*, D00A18, doi:10.1029/2008JD009982.

Szyrmer, W., and I. Zawadzki (1999), Modeling of the melting layer. Part I: Dynamics and microphysics, *J. Atmos. Sci.*, *56*, 3573–3592.

Tanelli, S., S. L. Durden, E. Im, K. Pak, D. Reinke, P. Partain, J. M. Haynes, and R. Marchand (2008), CloudSat's cloud profiling radar after 1 year in orbit: Performance, calibration, and processing, *IEEE Trans. Geosci. Remote Sens.*, in press.

J. M. Haynes, T. S. L'Ecuyer, G. L. Stephens, and N. B. Wood, Department of Atmospheric Science, Colorado State University, Fort Collins, CO 80523-1371, USA. (haynes@atmos.colostate.edu; tristan@atmos.colostate.edu; stephens@atmos.colostate.edu; norm@atmos.colostate.edu)

S. D. Miller, Cooperative Institute for Research in the Atmosphere, Colorado State University, Fort Collins, CO 80523, USA. (miller@cira.colostate.edu)

C. Mitrescu, Naval Research Laboratory, 7 Grace Hopper Avenue, Stop 2, Monterey, CA 93943, USA.

S. Tanelli, Jet Propulsion Laboratory, California Institute of Technology, 4800 Oak Grove Drive, Pasadena, CA 91109, USA. (simone.tanelli@jpl.nasa.gov)